PAPER

Check for updates

Morphology control of SERS-active 2D gold nanosnowflakes†

Sullivan Cohen-Pope,‡ John R. Crockett,‡ Maggie Wang,‡ Kaitlyn Flynn, Alexandra Hoff and Ying Bao [ID] *

Two-dimensional (2D) gold-branched nanomaterials such as nano-snowflakes or nano-dendrites have previously been demonstrated as promising candidates for surface-enhanced Raman scattering (SERS) substrates and catalysis. Herein, we present a rapid and effective synthesis method for preparing 2D gold nanosnowflakes (Au NSFs) where pre-existing seeds in the growth solution act as nucleation centers and avoid new nucleus formation. Methods to fine-tune the morphology and size of the 2D Au NSFs by adjusting the synthesis conditions are also explained, along with the discussion of a proposed formation mechanism to explain the experimental data on morphology formation. In addition, the optical properties of various controlled morphologies of 2D Au NSFs are explored and the SERS performance is investigated to study the relationship between the substrate local environment and SERS enhancement. This work not only involves the preparation of SERS active 2D Au NSFs with controlled morphology, but also provides a deeper understanding of dendritic formation.

Introduction

Morphology controlled synthesis of gold nanomaterials has been attracting extensive attention in recent years since the size and shape of these nanomaterials can greatly influence their optical, electronic and chemical properties.[1–3] These properties determine the usefulness of the nanomaterials in a wide range of applications, such as catalysis,[4] bio-sensing,[5] optics,[6] solar cells,[5] bioimaging,[7] and surface-enhanced Raman spectroscopy (SERS).[8,9] A variety of shapes can be produced, including spheres, cubes, rods, plates, *etc.*, which allows for the selection of desired properties for specific applications.[10–12] From this wide variety, 2D branched nanostructures (*e.g.* dendritic, snowflake, and flower-like) have attracted significant attention, particularly in the fields of SERS and catalysis. These nanostructures have large specific surface areas and a high density of edges and corners, which are essential features for SERS and catalyst performance.[13–16]

Until now, most reported 2D Au branched nanostructures have been fabricated at interfaces, such as air/water, liquid/liquid and solid/liquid.[14,17–20] Compared to other nanostructure types, constructing 2D branched nanostructures has a unique synthetic challenge, which is to confine the branching to one plane while minimizing growth in the perpendicular direction.[20] The studies that have managed to synthesize such nanostructures[19,21,22] have utilized methods such as electrochemical deposition[17] and galvanic reactions.[20,21] While these approaches have been demonstrated to permit direct fabrication of branched nanomaterials on substrates, these methods have also resulted in minimal control on the location and the quantity of gold ions being reduced. Control of these parameters is essential for influencing the nucleation and growth kinetics of nanocrystals and their subsequent impact on the final morphology.

Several other research groups have put effort into preparing 2D Au dendrite nanostructures with the assistance of structure-directed surfactants or additives and have demonstrated some level of control of the shape of 2D Au dendrite nanomaterials, though these groups have not simultaneously controlled the shape, size and density.[23,24] For example, Wang and co-workers fabricated 2D snowflake-like highly branched Au nanostructures with the aid of the cationic gemini surfactant, hexamethylene-1,6-bis(dodecyl dimethylammonium bromide) ($C_{12}C_6C_{12}Br_2$). In their work, $C_{12}C_6C_{12}Br_2$ acted as a capping agent which was selectively adsorbed onto the (111) plane to drive the generation of the 2D morphology. Additionally, the surfactant also played a role in mediating the growth kinetics through the quaternary ammonium cations of $C_{12}C_6C_{12}Br_2$ binding with both Au(III) and Au(I) through strong electrostatic interactions. This led to a decrease in the reduction potential of the gold ions and a decrease in the diffusion rate, resulting in some control of the shape (though not the size or density) of Au 2D branched nanostructures.[24]

Department of Chemistry, Western Washington University, Bellingham, WA 98225, USA. E-mail: ying.bao@wwu.edu

† Electronic supplementary information (ESI) available: Additional STEM images, chemical reactions, videos of sample preparation under various pH conditions, UV-vis spectra, and optical images. See DOI: 10.1039/d0tc02183k

‡ These authors have contributed equally to this work.

Seed mediated growth is widely used to control the morphology of branches for 3D Au nanostructures by altering the ratio of gold seeds and chemicals in colloidal growth solution.[25] The seeds in the growth solution can act as nucleation centers, favoring exterior gold atoms to be immobilized on the surface, slowing the formation of new nucleation centers. In addition, by altering the ratio of seeds and additive chemicals in the growth solution, it is possible to control the diffusion kinetics of metal ions and thus the reactivity of the gold ions. For example, Li and co-workers altered the ratio of the gold seeds and the additive hydroquinone, allowing for a wide range of tunability in the diameters and morphologies of urchin-like Au particles.[26] Even with such an approach being commonly used in colloidal solution synthesis, there is no report on using such an approach to fabricate 2D dendrites with controlled sizes, shapes and densities.

In this work, we have developed a simple and rapid synthesis method for 2D gold nanosnowflakes (Au NSFs) based on seed mediated growth which allows for fine-tuning of the morphology and size of the 2D Au branched structurers by altering the synthesis conditions. Gold nanoparticle seeds were pre-placed on the substrate, and then a reduction mixture of sodium citrate and hydroquinone was used to form the Au NSF, which acts as reducing agents and capping ligands. The Au^{3+} is reduced to Au^+ by citrate, while Au^+ is further reduced to Au^0 by hydroquinone. The impacts of seed concentration and growth solution pH on the resulting Au NSFs were explored in detail, and a mechanism of the Au NSF formation is proposed based on the experimental data on both morphology formation and evolution. The optical properties of various controlled morphologies of 2D Au NSFs were explored. Finally, we investigated the relationship between the substrate local environment and SERS enhancement *via* conducting optical imaging and confocal Raman mapping of same area which gives us a better understanding of the structure–property relationship.

Results and discussion

Synthesis and characterization of 2D polymer–Au NSF composites

The approach to preparation of polymer–Au NSF composites starts from a piranha solution treated substrate as shown in

Scheme 1. In order to fix the gold seeds onto the substrate, the substrate was modified by alternating charged polyelectrolytes and by eventually leaving the positively charged polymer as the top exposed layer. The gold seeds can thus be fixed on the modified substrate *via* electrostatic attraction. In this case, 1.5 bilayers of polyelectrolytes were deposited on the substrate before further use. The pre-placed gold nanoparticle seeds with diameters of 15.0 ± 2.4 nm were prepared by reducing gold chloroauric acid with sodium citrate at boiling temperature.[27] The pre-placed seeds were then grown into the NSF structures by immersing the substrate into the growth solution. To kinetically control the formation of Au^0 atoms and subsequent Au crystal, weak reducing agents including sodium citrate and hydroquinone were employed under the growth conditions. The whole process is completed under 4 minutes, which is very rapid. Note that there are two steps to complete the process of creating and stabilizing Au NSFs. The first step is the reducing process which takes two minutes to complete. Such a reaction time is determined by monitoring the growth of the Au NSF. If the permitted reaction time was substantially reduced, the Au nanostructures would not have reached their maximum size given the synthesis conditions. The second step is the additional injection of hydroquinone and reaction for two additional minutes. This step is to allow hydroquinone to fully stabilize the branch formation. The ligand stabilization is a very quick process. As others have reported,[28] the UV spectra were unchanged with two minutes of the ligand addition. It is worth mentioning that during the formation of nanoflakes, the seeds will behave as an active surface for exterior gold atoms to deposit. The size of the seed might have a minor impact on the core-size of Au NSFs, while it would not largely impact the morphology of the Au NSFs.

Fig. 1a shows the scanning electron microscopy (SEM) image of the fabricated NSFs under the default synthesis conditions, revealing their morphology, structure, and size. It is clearly seen that the fabricated Au NSFs were deposited across the film without any significant aggregation. Fig. 1b (and Fig. 1b inset with larger magnification) shows the morphology of individual Au NSFs: rather symmetric dendritic nanostructures with pronounced branches originating from the core and then split into larger numbers of sub-branches filling the space at the boundaries. Atomic force microscopy (AFM) was used to measure the thickness of the Au NSFs. As shown in Fig. 1c, the thickness of Au NSFs is relatively uniform. Note that the core of
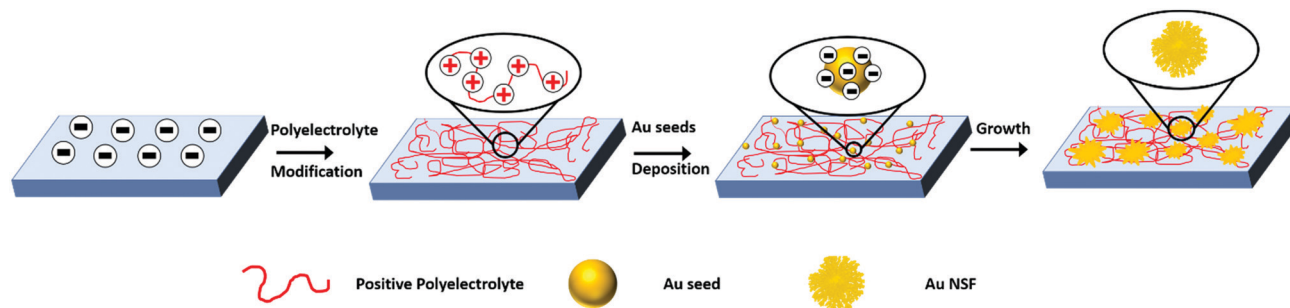
Scheme 1 Schematic illustration of the polymeric–gold nano-snowflake (Au NSF) composite preparation.
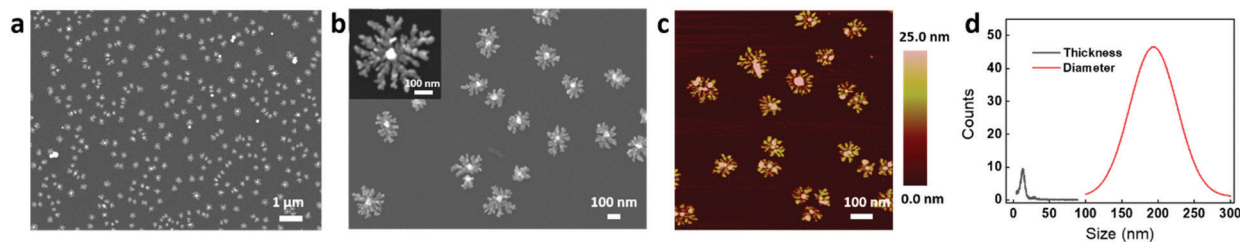
Fig. 1 SEM images of the as-prepared NSFs with (a) low magnification and (b) higher magnification (the inset in b shows the dendrite nanostructure of the individual NSF). (c) Height AFM image of the fabricated NSFs on the polymer modified substrate shows the thin thickness of the NSFs. (d) Data histograms of NSFs' thickness (black line) and diameter (red line).
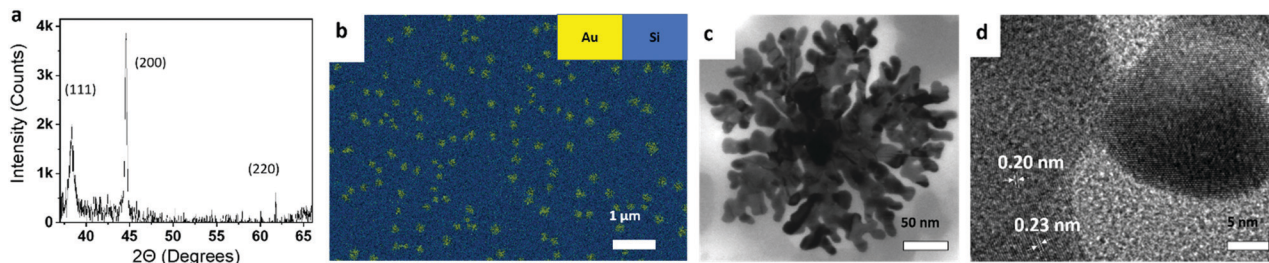

Fig. 2 Characterization of the as-prepared NSF on the polymer modified Si wafer: XRD pattern (a), elemental mapping (b), TEM and the corresponding HRTEM images (c and d). The exposed lattice fringes are the (111) plane and (200) plane, corresponding to the Au lattice spacings of 0.23 nm and 0.20 nm, respectively.

the Au NSF is much thicker than the branches. One representative AFM image of an individual NSF with height profile is provided in the ESI† (Fig. S1) showing that the thickness of the NSF core is about 40 nm more than the branches. Additionally, the branches of the NSF are not completely flat and the thinnest branch is less than 10 nm tall. Based on AFM and SEM data, the average diameter of the Au NSFs under our default synthesis conditions was found to be 194.4 ± 37.6 nm and the average thickness was about 12 nm. The size and thickness histograms are shown in Fig. 1d (red and black traces, respectively). Thus, the aspect ratio of the Au NSFs is well above 15, which indicates that the structure is 2D.

Fig. 2a presents the X-ray diffraction (XRD) pattern of the as-prepared NSFs on the polymer modified Si substrate which reveals its crystalline information. There are clearly observed main diffraction peaks at *ca.* 38.2° and 44.4° assigned to the (111) and (200) lattice planes of face-centered cubic (fcc) Au crystal (JCPDS No. 4-0784). In addition, the diffraction peak at *ca.* 64° assigned to the (220) lattice planes is quite weak and cannot be well discerned. The single crystalline domains, determined by the Debye–Scherrer formula, were 16.60 nm and 40.02 nm according to the (111) and (200) crystalline planes, respectively. It is understandable that (111) gives a smaller crystalline size since the sharpness of the diffraction peaks correlates with the size of the crystallite. It is interesting to note that the intensity ratio of the (111) peak to the (200) peak is *ca.* 0.5. This value is substantially smaller (specifically speaking, nearly 4 times) than is reported in the standard JCPDS file of Au,[29] which generally is *ca.* 2. Such an observation indicates that the as-prepared Au NSFs shown in Fig. 1 are

polycrystalline in nature and are predominantly enriched with (200) crystal facets. Elemental analysis was performed by energy dispersive X-ray spectroscopy (EDS) elemental mapping (Fig. 2b) and confirms the active presence of silicon as the substrate and further confirms that NSFs are composed of elemental Au.

In order to perform high-resolution transmission electron microscopy (HRTEM) to further verify the population of crystal planes in the Au NSFs, freestanding NSFs were fabricated by adding a sacrificial layer of cellulose acetate on the substrate before the polyelectrolyte modification and increasing the numbers of polyelectrolyte bilayers before seed deposition. The detailed preparation of the freestanding film is stated in the Experimental section. Fig. S2 (ESI†) shows the Au NSFs fabricated on 18.5 bilayers of polymeric thin films composed by alternating deposition of positively and negatively charged polyelectrolytes. It can be clearly observed that the polymeric thin film, which is porous, is decorated with a high density of Au NSFs. The porous structure of the thin film is possibly due to the low concentration of the polymer that was applied in this study. It is worthwhile to note that the Au NSFs are less likely to grow over the top of pores, instead tending to grow around them, as seen in Fig. S2 (ESI†). In addition, the density and size of pores on the thin film can be controlled by carefully modulating the conditions of the assembly process and post-treatments of thin films according to previous studies.[30] The size and morphology of Au NSFs are consistent with the ones that were constructed on few layers of polymer modified silicon wafers. The Au NSFs are composed of numerous branches and their formed nanogaps, as seen in Fig. 2c. The corresponding HRTEM image of an individual Au NSF is shown in Fig. 2d.

Crystalline lattice fringe spacings of 0.20 nm and 0.23 nm, assigned to (200) and (111) facets of fcc Au, can be easily observed. This observation is in good agreement with the data obtained from XRD investigation showing that the Au NSFs are polycrystalline.

Mechanistic study of the formation of Au NSFs

It has been reported that 2D nanostructures, including nanoplates and nanodendrites, can be formed under kinetically controlled conditions, where the driving force is large, through a non-equilibrium process.[31] The main criterion proposed to achieve kinetic control is that the reaction should proceed considerably slower than under normal conditions. Under such conditions, the final product can take on shapes deviating from the thermodynamically favored equilibrium shape. Therefore, the formation of more complicated structures requires a higher driving force, *i.e.*, a lower reaction or precursor rate. In our work, the growth of 2D Au NSFs is carried out by kinetically controlled reduction by using weak reducing agents including sodium citrate and hydroquinone under the growth conditions. In addition, the whole nanostructure formation process is under the guidance of a "diffusion-limited aggregation" (DLA) strategy as depicted in Scheme 2.

The substrate initially has deposited Au NP seeds acting as the nucleus, which are the growth centers for the final products. A reduction mixture of sodium citrate and hydroquinone is used to stepwise reduce Au^{3+} to Au^0. Since the growth step is operated at room temperature, the reducibility of sodium citrate is weak which can only reduce Au^{3+} to Au^+. When hydroquinone was added, the Au^+ was slowly reduced to Au^0 which was then migrated onto the substrate where aggregation with the existing Au seeds leads to the formation of the primary branches.[26]

With continuous reduction of Au^{3+}, more Au^0 is formed far from Au cores and diffuses across the substrate to further join the core at places with a lower energy barrier to form secondary and higher order branches. The process will last until all Au^{3+} ions are consumed. Eventually, the DLA process facilitates the assembled nanostructure as a dendrite-like fractal structure. The formed nanostructure was stabilized by the excess sodium citrate, adsorbing on the Au surface. Note that hydroquinone might also adsorb on the Au surface, in direct competition with sodium citrate. However, given that sodium citrate possesses stronger coordination with the gold surface than does hydroquinone, it acts as the primary ligand.[26,32]

Control over the density, size and microfeatures of the NSFs

From the above discussion, it can be expected that both the morphology and size of 2D Au NSFs will be greatly influenced by the number of pre-deposited seeds on the surface of the polymer modified substrate as well as by the growth rate of NSFs' branches. Both of these can be fine-controlled by the experimental design.

Pre-seed concentration. Variations in the Au seed concentration deposited onto the polymer modified substrate were studied in order to observe the morphology change of the fabricated Au NSFs. Fig. 3a shows the Au NSFs fabricated when the seed solution was 45 times (45×) diluted with nanopure water, which reduces the concentration of Au seeds from 0.71 mM (found from 3× dilution under the default synthesis conditions) to 0.047 mM. The silicon substrate is uniformly decorated with much larger 2D Au NSFs (diameter ∼ 1000 nm, as compared to ∼194 nm under the default conditions) without any significant aggregation; Fig. 3b shows a representative SEM image of an individual Au NSF. It can be clearly observed
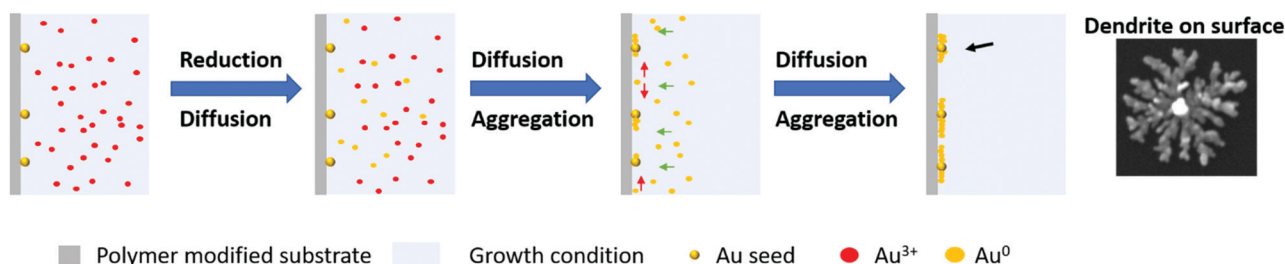
Scheme 2 A schematic illustration of the Au NSF formation process.
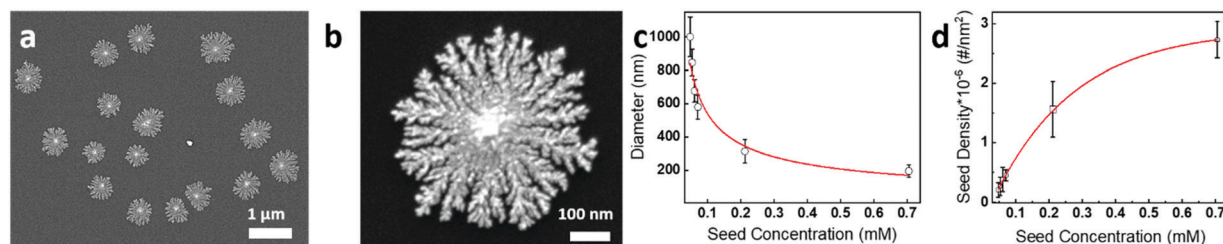

Fig. 3 SEM images of Au NSFs fabricated with a seed concentration at 0.016 mM with low magnification (a) and high magnification (b). (c) Plot of Au NSF average diameter *vs.* seed concentration. (d) Plot of seed density on the substrate *vs.* seed concentration.

by comparison to the Au NSFs fabricated from 0.71 mM seed solution (3× diluted, shown in Fig. 1b) that the Au NSF grown from a lower concentration of seed has a bigger core and more complex branches with nanosized roughness features. This can be explained by the decreased Au seed nucleus concentration, which leads to additional gold atoms for deposition onto each of the seeds, thereby forming more branches. EDX elemental mapping (Fig. S3, ESI†) reveals that the NSF is still entirely composed of elemental Au.

Fig. 3c clearly shows that as the seed concentration was diluted, the average size of Au NSFs increased. For instance, when the seed concentration was diluted by 10×, the average size of Au NSFs was 314 nm. As the concentration was diluted further to 30× (0.0705 mM), the average size of Au NSFs increased to 580 nm. Eventually, with 45× dilution, the average size of Au NSFs reached about 1000 nm. We found that the size of Au NSFs increases nonlinearly with a decrease in the seed concentration. Such results can be explained by the impact of concentration of the seed solution on the density of the seed that was deposited onto the substrate. The densities of seeds deposited onto the substrate decreased exponentially with increased dilution, as can be seen in Fig. 3d. The seed density on the substrate increases nonlinearly with the concentration of the seed solution. The trend in seed density mirrors the change of the NSF diameter, indicating that a higher density of seeds on the substrate will lead to smaller NSF growth. This is reasonable, since the gold source concentration remains the same in our study, and so the number of seeds will determine the amount of source gold that could be consumed by individual seeds. With more seeds, less gold source will be available for individual seeds.

pH effect. The effect of adjusting the pH of the growth solution on the morphology of Au NSFs was studied. The pH of the growth solution was adjusted from the default synthesis conditions of pH 3.10 by adding either HCl or NaOH over the pH range of 1.69 to 4.97. As the pH of the solution was decreased to 1.69, the color of the growth solution changed slower while at higher pH, the color change was more rapid. As shown in videos (Video S1, ESI†), upon the addition of hydroquinone, the initially colorless growth solution at pH 1.69 takes 20 s to turn orange. When the growth solution has a pH of 3.10, which is the default growth solution, it takes 2 s to undergo a rapid color change from colorless to brown (Video S2, ESI†). In the case of pH 4.97, the color changes almost instantly from colorless to dark blue (Video S3, ESI†). The growth solutions

from pH 1.69 and 4.97 after the reactions were examined by using a UV-Vis spectrometer and their spectra show a distinctive difference. Specifically, the pH 4.97 growth solution shows broad plasmon resonance features starting at 700 nm (Fig. S4, ESI†), which has a high absorption intensity. It is highly indicative of excess gold nanoparticle formation in the growth solution. Meanwhile, the UV-Vis spectrum of pH 1.69 growth solution only shows a very weak peak at 420 nm. This indicates that the gold sources in the solution are almost entirely immobilized on the substrate, leave nearly zero gold in the solution.

SEM imaging was used to analyze the different morphologies of the Au NSFs prepared in various pH growth solutions. Fig. 4a, b and Fig. S5(a–f) (ESI†) show the representative SEM images of Au NSFs prepared in various pH growth solutions. An important feature of all samples is that the individual branches from two neighboring seeds never crossed each other, instead, a small but clear gap was formed at the converged interface. This is caused by the deficiency of the gold source at this location. Beyond this, based on the SEM images, the morphologies of NSFs from pH 1.69 to pH 4.97 appear significantly different. The Au NSFs on substrates appears more uniform on samples prepared at the pH toward acidic conditions. As shown in Fig. S6 (ESI†), a sample prepared at pH 1.69 shows much higher density of Au NSFs across the substrate. Compared to the default sample prepared at pH 3.10 (in Fig. 1a), the structure in Fig. 4a tends to have fewer branches and the diameter of the Au NSFs is larger, about 441 ± 119 nm. The gap between two Au NSFs due to deficiency of gold sources between them occurs more frequently in this sample since the NSFs are larger and tend to get close to neighboring seeds as clearly shown by the two highlighted sectors in Fig. 4a.

However, the sample prepared at pH 4.97 has less uniformity. In addition to snowflake nanostructures on the substrate, there are 'popcorn-like' gold nanomaterials. Such structures were observed on samples prepared from pH 3.20 to 4.97, as clearly shown in Fig. S5(e and f) (ESI†) and inset in Fig. S5g (ESI†). The sizes of the popcorn-like nanomaterial were analyzed and showed no significant difference among these samples, about 90 nm in diameter on average (Fig. S5g, ESI†). The structure of Au NSFs prepared at pH 4.97 shows more branches (shown in Fig. 4b) and the diameter of the Au NSFs is larger, about 592 ± 121 nm, compared to the default sample prepared at pH 3.10. Note that the NSFs shown in Fig. 4a are much denser than those shown in Fig. 4b, which can cause NSFs shown in Fig. 4a to appear larger
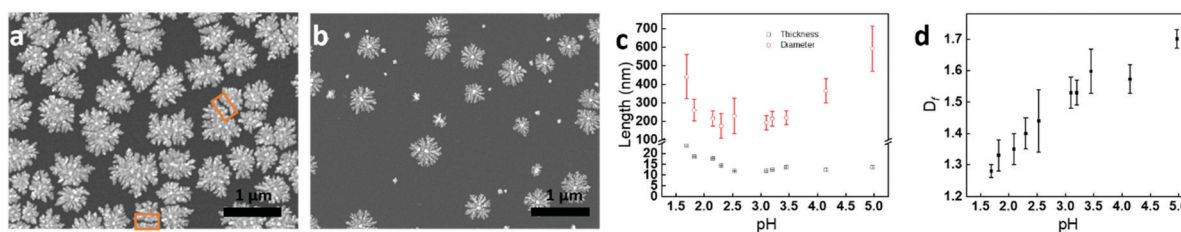

Fig. 4 SEM images of Au NSFs fabricated with pH of growth solutions at (a) 1.69; (b) 4.97. (c) Average length with respect to the diameter and thickness of the Au NSFs under various pH growth conditions. (d) Plot of fractal dimension vs. pH of growth solutions.

than they are. Fig. 4c shows the Au NSFs' diameter and thickness under various pH growth conditions. Note that Fig. 4c does not include data for the popcorn-like nanomaterial when it exists from pH 3.20 to 4.97. It clearly shows that the diameter of Au NSFs increases when decreasing the pH from 3.10 to 1.69 and increasing the pH from 3.10 to 4.97. The thickness of the Au NSFs, obtained from AFM, decreases when increasing the pH from 1.69 to 2.53 and maintains relatively similar thickness afterwards.

The fractal pattern can be analyzed as an index of fractal dimension (D_f). D_f describes their convolution in the ratio of change in detail to that of scale, which provides the information about the structural complexity and its efficiency, specifically in terms of the covered surface area.[33] D_f is calculated by the box counting method following Barabasi (details in the ESI†).[34,35] We used the fractal dimension D_f to evaluate the shape complexity of Au NSFs, calculating them using Fraclac Version 2.5 software developed by A. Karperien.[36] The calculated values of D_f for NSFs from pH = 1.69 to 4.97 are shown in Fig. 4d. It was found that when pH increased from 1.69 to 4.97, the D_f gradually increased from 1.28 ± 0.02 to 1.70 ± 0.03. This indicates that with increasing pH, the branching of fractal structures increases, which can also be observed from the SEM images. We note that the value of $D_f = 1.70 \pm 0.03$ for the pH 4.97 sample is in agreement with the 2D DLA simulation (ca. 1.7).[37,38]

Based on these results, we suggest that the supply rate of Au^0 under higher pH growth conditions is much faster than that under lower pH growth conditions. Sodium citrate and hydroquinone are well known reducing agents whose electrochemistry and impact on the synthesis of gold nanomaterials have been widely studied.[39–41] During reduction, sodium citrate firstly reduces Au^{3+} to Au^+ by accepting two electrons from the citrate oxidation reaction. Once Au^+ is formed, hydroquinone reduces them to Au^0. Hydroquinone undergoes a two electron, two proton oxidation process to form benzoquinone which is illustrated in Fig. S1 (ESI†). The influence of pH on the oxidation of reducing agents is important because H^+ ions are involved in the oxidation/reduction process.

When HCl is added to lower the pH of the solution, it provides H^+ ions to the solution. As the number of H^+ ions increases, the availability of electrons to reduce the Au^{3+} decreases and the reaction rate becomes slower. In accordance with Le Chatelier's principle, citrate and hydroquinone become less effective in reducing processes and the Au^0 formation rate becomes much slower. In this case, the surfaces of the gold seeds probably play a more important role as surface-catalyzed centers, which favor the exterior gold atoms to reduce on the seeds' surface. Given the less effective oxidation process, hydroquinone prefers reducing Au^+ on the surface of gold seeds. This also can explain why the thickness of Au NSFs increases when decreasing the pH of the growth solution. In addition, due to the slow diffusion and deposition rate, the final Au NSFs have fewer branches and their D_f is about 1.28, which is far away from 2D DLA simulation (ca. 1.7).

On the other hand, under the higher pH conditions, the rate of Au^0 reduction increased which makes secondary nucleation unavoidable. In this case, the surfaces of the gold seeds probably play a less important role as surface-catalyzed centers. Instead, hydroquinone is able to reduce Au^+ to Au^0 far from Au cores and Au^0 diffuses across the substrate to further join the core which was discussed in Scheme 1. Since the Au^0 is produced much faster than it is consumed by the Au seeds, secondary nuclei are formed in solution. The observed popcorn-like objects are the resulting nanomaterials formed in solution and deposited on the substrate and give rise to the Au formation peak. Additionally, this increased rate of Au^0 reduction explains the fast color change of the growth solution discussed earlier. A potential explanation for the popcorn-like objects being of similar size is that sodium citrate stabilized the gold, restricting the nanoparticle growth to a critical size. Under higher pH conditions, in addition to being a source for secondary nucleation formation, there is enough Au^0 in the solution to continue to deposit on the surface of gold seeds, forming NSFs via DLA growth. The change of D_f values also suggests that the formation of the higher branched Au NSF (with higher D_f) occurs with high immobilization efficiency of Au^0 on pre-placed seeds.

The XRD patterns shown in Fig. 5 are analysed to acquire the structural information of NSFs fabricated under various pH conditions. The XRD patterns of samples fabricated from growth solutions at pH 4.97 and 1.69 are shown in Fig. 5a. It is obvious that the (111) crystal facets are highly exposed as seen from the extremely high (111) intensity for both samples. Very high values of the intensity ratio of (111)/(200) suggest that the (111) facets are predominantly enriched in the samples. One clear difference between the samples from pH 4.97 and 1.69 shown in Fig. 5a as compared to the sample fabricated at pH 3.10 shown in Fig. 2a is that their diameters are larger, as seen in Fig. 4c. Thus, these observations suggest that the Au NSF grew preferentially along the (111) direction. Similar observations on Au dendrites were reported by other groups.[42,43] In addition, the sample fabricated at pH 1.69 is much thicker and denser than other samples. This explains the high counts for this sample compared to others. Fig. 5b shows the plot of peak ratio vs. pH of the growth solutions. The relationship between the diameter of the Au NSFs and populations of plane (111) is further confirmed by noting that the trend of populations of plane (111) as pH levels change seen in Fig. 5b is in agreement with the trends of the diameter and thickness of Au NSFs as pH levels change shown in Fig. 4c. In both these figures, the minimum value occurs around pH 3.10.
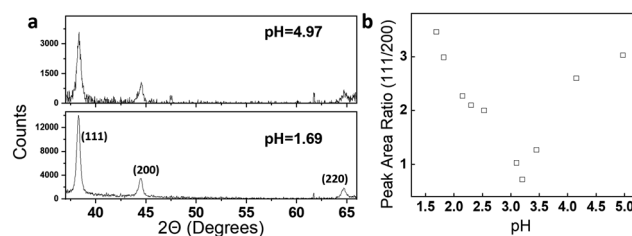

Fig. 5 XRD patterns of Au NSFs fabricated with pH of growth solutions at (a) 4.97 and 1.69. (b) Plot of the peak ratio (200/111) vs. pH.

Optical properties and SERS result

Fig. 6 shows the UV-vis-NIR spectra (400 nm to 1500 nm) of four represented samples that were fabricated under various conditions, including pH 1.69, 3.10, 4.97 and pH 3.10 but with pre-deposition of 45× diluted seed solution (instead of the 3× default). Note that the "squiggle" region in the spectra was due to the switching between diffraction gratings, which was unavoidable in the experiment. The default sample prepared at pH 3.10 showed strong absorptions at 580 nm. As is well known, the surface plasmon resonance (SPR) of the Au nanomaterial greatly depends on its morphology and environment. Thus, the observed absorption spectra may represent a contour combining the size, aspect ratio and coupling factors of the hierarchical dendritic structures. For Au NSFs, as the size of the 2D structure increases, the frequency of SPR will move to a longer wavelength due to the long-range interaction of SPR in the 2D NSFs. As shown in Fig. 6, samples prepared with pH 1.69 and 4.97 give a significant red-shift of the SPR peak from the visible to the near infrared region, which is consistent with the morphology evolution of NSFs discussed earlier. The broadened peaks may be the result of multiple plasmon coupling between side branches and neighboring trunks. It is worth mentioning that the broadened SPR peak for NSFs at pH 1.69 has another attribution since the sample prepared under these conditions has much 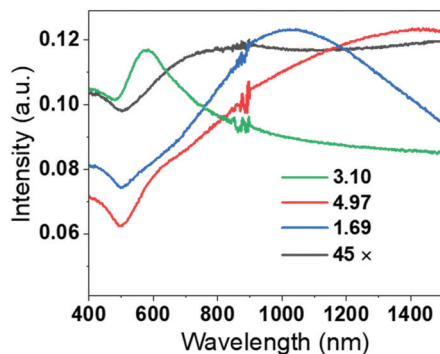denser packing of NSFs. Such dense packing can generate a significant amount of intra-structural plasmonic coupling, leading the plasmon resonance to broaden. For the sample prepared at pH 3.10 with 45× diluted seed solution, the spectrum shows a gradual increase in absorption from about 500 nm to the near-IR region without indication of leveling off. This is not surprising considering that the size of Au NSFs under these conditions is close to one micrometer and such broadened absorption can be ascribed to the dipole and quadrupole plasmon resonances of NSFs based on the prediction of discrete dipole approximation.[44,45]

It has been demonstrated that gold branched nanostructures present a great deal of sharp corners, edges and junctions, which act as electromagnetic "hot spots" for SERS. In our work, the SERS intensities for the fabricated substrates are not uniform across the substrates since the SERS intensity will be impacted due to local environments such as the size and density of Au NSFs on substrates.[46,47] Due to the non-uniform distribution of Au NSFs, it is not possible to obtain a representative EF and LOD for the prepared samples as reported elsewhere.[48–50] In order to understand the relationship between the substrate conditions and SERS properties, optical imaging and confocal Raman mapping were conducted on substrates decorated by the Au NFs obtained at pH 1.69. Rhodamine 6G (R6G) was used as a probe molecule. Fig. S7 (ESI†) shows the Au NSF-decorated substrate with a scratch, which is used to give contrast to the Au NSF area. The locations of the Au NSFs can be observed under an optical microscope which has a brighter color than the area without NSFs. A typical 10 μm × 10 μm area, shown in Fig. 7a, was investigated using the confocal Raman technique. The SERS mapping result in Fig. 7b shows that the intensity distribution of certain Raman peaks in this case is at 1507 cm^{-1} across the whole area. Strong SERS signals were obtained from the locations having Au NSFs. The Raman map shows a similar pattern to the optical image, indicating the effective SERS enhancement of Au NSFs on the substrates. In other words, the Raman map identified the location and density of the Raman hot spots, which were generated by closely packed Au NSFs.

Three Raman spectra from the represented spots (red, blue, and black color in (b)) were plotted and are shown in Fig. 7c. Compared to the spectrum taken on the black spot without Au
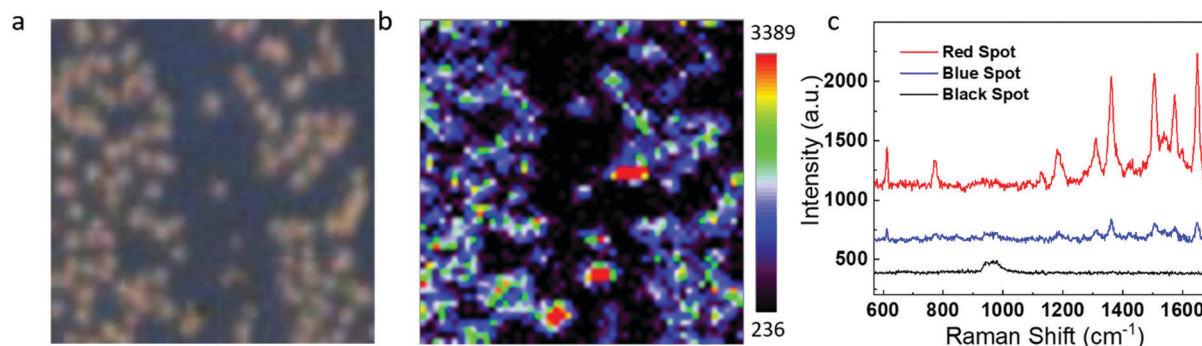

Fig. 6 Normalized optical extinction spectra of Au NSFs fabricated under pH 1.69, 3.10, and 4.97 as well as 45 times diluted seed solution with pH 3.10.

Fig. 7 (a) The optical image of the Au NSF decorated substrate with a scratch; (b) confocal Raman image of the same area. Size of the area: 10 μm × 10 μm. (c) Raman spectra recorded in positions (red, blue and black spots) in (b).

NSFs, the red and blue areas show the characteristic vibration bands of R6G molecules which clearly appeared at 612, 765, 1186, 1306, 1360, 1508, 1574, and 1650 cm^{-1}. The band at 612 cm^{-1} was assigned to the ν(C–C–C) in-plane stretching mode. The bands at 765 and 1186 cm^{-1} were assigned to the ν(C–H) out-of-plane and in-plane bend mode, respectively. The bands at 1360, 1508, 1574, and 1650 cm^{-1} were related to the C–C stretching of the aromatic ring.[51] The black spot does not have any characteristic peaks of R6G which is reasonable due to the lack of Au NSFs. Additionally, the red spot has much stronger SERS intensity than the blue spot. By comparing the optical image and SERS mapping, it can be observed that the red spot is coming from the locations that have several Au NSFs while blue spots have lower NSF density. Thus, the ability to observe strong SERS signals from one or a small number of Au NSFs is valuable for both the fundamental study of SERS-active substrates and potential applications such as sensing technology.

Conclusions

In summary, an efficient approach to fabricate 2D Au snowflake-like nanostructures on polymeric modified substrates has been demonstrated where the morphology of the nanostructure can be controlled and fine-tuned by adjusting the density of seeds and the pH of the growth solution. This seed mediated growth approach is effective in controlling the number of nuclei on the substrate and thus controlling the final morphology formation. SERS characterization was performed to study the relationship between the substrate local environment and SERS enhancement. Our study demonstrated a successful approach to fabricate SERS-active dendrite 2D Au nanostructures with controlled morphology, structures, and properties, which will have broad applications in fields such as plasmonics and catalysis.

Experimental section

Chemicals and materials

Tetrachloroauric acid trihydrate (HAuCl$_4$·3H$_2$O, $\geq$99.9%), hydroquinone ($\geq$99%), sodium hydroxide (NaOH, 30 wt%), hydrogen peroxide (H$_2$O$_2$, 30 wt%), crystal violet (CV), cellulose acetate (CA, MW $\approx$ 30 000), poly(allylamine hydrochloride) (PAH, MW $\approx$ 50 000) and poly(sodium 4-styrenesulfonate) (PSS, MW $\approx$ 70 000) were purchased from Sigma-Aldrich. Hydrochloric acid (HCl, concentrated) was purchased from Macron. Ethanol (95%) was purchased from Pharmco-Aaper. Sodium citrate dihydrate (C$_6$H$_5$O$_7$Na$_3$·2H$_2$O, $\geq$99%) and sulfuric acid (H$_2$SO$_4$, concentrated) were purchased from Fischer. Poly(diallyldimethylammonium chloride) (PDADMAC, MW $\approx$ 240 000) was purchased from Polysciences. Nanopure water with a resistivity of 18 MΩ cm was used in all experiments.

Preparation of seed solution

Negatively charged citrate-coated gold nanoparticles (Au NPs, 13 nm in diameter) were prepared according to the well-known citrate reduction method as described in the literature.[52]

Typically, HAuCl$_4$ (75 μL, 0.1 M) was added to nanopure water (30 mL) and brought to a boil on a stir plate. Then, sodium citrate (900 μL, 1 wt%) was added to the solution and left to boil for 40 minutes. A few minutes after the sodium citrate was added, the solution turned from clear to lavender, before finally turning to wine red. The resulting seed solution was allowed to cool to room temperature, and then was stored in a fridge for further use. Under the default conditions, the seed solution was diluted three times before use.

LBL thin film preparation

Silicon-wafer substrate and glass slide substrate with a typical size of 10 mm × 10 mm were cleaned using a piranha solution [3 : 1 (v/v) H$_2$SO$_4$/H$_2$O$_2$]. **Attention**: piranha solution is extremely dangerous and should be handled very carefully. After cleaning, the substrates were rinsed with nanopure water at least three times and then stored in nanopure water until use. The glass slide substrates were used for the purpose of obtaining UV-Vis spectra of Au nano-snowflakes. The multiple polymer layers were fabricated by the spin-assisted LbL method. In general, a layer of a positively charged polyelectrolyte was first deposited onto the substrate by spin coating for 30 s at 11 000 rpm. The substrate was rinsed once with nanopure water and dried while spinning for 30 s at 11 000 rpm. In a similar manner, a negatively charged polyelectrolyte was deposited. This procedure was repeated until the desired number of polymer bilayers was achieved. Two types of polymer bilayers were prepared. One has 1.5 bilayers which were fabricated with PDADMAC (0.1 wt%) and PSS (0.3 wt%), expressed with the formula: PDADMAC/PSS/PDADMAC; the other has 18.5 bilayers which were fabricated with PAH (0.2 wt%) and PSS (0.2 wt%), expressed with the formula: (PAH/PSS/PAH)$_{18.5}$ and it is for the freestanding film. After fabricating the designed polymer bilayers, 200 μL of the sodium citrate gold nanoparticle solution with certain dilution was deposited on the substrate by spin coating for 30 s at 11 000 rpm. To obtain a freestanding film, a sacrificial cellulose acetate (CA) layer was first spun on the prepared silicon substrate before further deposition. Freestanding LbL thin films can be obtained by dissolving the sacrificial CA layer in acetone. The freestanding LbL films can be lifted from the solution using a variety of substrates, such as glass slides, silicon wafers, and copper grids for further characterization and investigation. All of the procedures were performed in a class 100 softwall clean room.

Gold nano-snowflake growth

For the nano-snowflake growth, HAuCl$_4$ (75 μL, 0.1 M) was added to nanopure water (9.6 mL) in a 20 mL vial. The pH of the solution was adjusted as desired using NaOH (4–30 μL, 1 M) or HCl (20–480 μL, 1 M). The seeded substrate was suspended in the solution, and then sodium citrate (22 μL, 1 wt%) was added, followed by hydroquinone (1 mL, 30 mM). After two minutes, another addition of hydroquinone (500 μL, 1 M) was performed. After another two-minute period, the substrate was removed from the solution and rinsed with nanopure water before being blown dry with nitrogen.

Instruments and measurement

We have utilized a variety of techniques to study the Au NSFs. The UV-visible spectra of Au NSFs were obtained using a Jasco V-670 UV-Vis-NIR spectrometer. The morphology and thickness of Au NSFs and multilayer thin films were measured on a Bruker BioScope Catalyst atomic force microscope using tapping mode under ambient conditions. The scanning electron microscopy (SEM) and scanning transmission electron microscopy (STEM) images of the freestanding multilayer thin film with Au NSFs were obtained using a JEOL-7200F field emission SEM operated at 30 kV. Higher resolution TEM (HRTEM) images were obtained using a FEI Tecnai F20 instrument (Thermo Fisher Scientific) operated at 200 kV. Samples for this analysis were prepared by depositing the freestanding films on copper grids and dried overnight.

The crystalline formation of Au NSFs was checked using a Rigaku Miniflex 6G benchtop diffractometer. The X-ray diffraction (XRD) patterns of Au NSFs on silica substrates were measured in the range of 32–90° with a step of 0.02° and a scan rate of 0.50° min^{-1} while spinning the samples at 10 rpm, employing characteristic Cu Kα radiation having a wavelength of k = 1.540593 Å, with a 40 kV voltage and 15 mA current. The full-width at half-maximum (FWHM) from different peaks was used in Scherrer's equation to determine the average crystallite size of the nanoparticles.

Rhodamine 6G (R6G) molecule was used as a Raman reporter to evaluate the SERS efficiency of the Au NSFs. Samples were prepared by dipping in 1 mM R6G solution for several hours and then substrates were dried overnight. SERS measurements were carried out with confocal Raman microscopes. The excitation wavelength was 532 nm, and the power was 200 μW. The spectrum was collected with a 50× objective and with 5 s integration time using a Thermo Scientific DXR2 confocal Raman microscope. SERS mapping results were collected with a 100× objective and with 5 s integration time using a Renishaw InVia confocal Raman microscope.

Conflicts of interest

There are no conflicts to declare.

Acknowledgements

References

1 K. L. Kelly, E. Coronado, L. L. Zhao and G. C. Schatz, *J. Mater. Chem. B*, 2003, **107**, 668–677.

2 C. Burda, X. Chen, R. Narayanan and M. A. El-Sayed, *Chem. Rev.*, 2005, **105**, 1025–1102.

3 M. Wang, A. Hoff, J. E. Doebler, S. R. Emory and Y. Bao, *Langmuir*, 2019, **35**, 16886–16892.

4 J. Zeng, Q. Zhang, J. Chen and Y. Xia, *Nano Lett.*, 2010, **10**, 30–35.

5 F.-J. Fan, L. Wu and S.-H. Yu, *Energy Environ. Sci.*, 2014, **7**, 190–208.

6 J. Xue, Z.-K. Zhou, Z. Wei, R. Su, J. Lai, J. Li, C. Li, T. Zhang and X.-H. Wang, *Nat. Commun.*, 2015, **6**, 8906.

7 P. Bian, J. Zhou, Y. Liu and Z. Ma, *Nanoscale*, 2013, **5**, 6161–6166.

8 X. Zhang, X. Xiao, Z. Dai, W. Wu, X. Zhang, L. Fu and C. Jiang, *Nanoscale*, 2017, **9**, 3114–3120.

9 Y. Bao, L. Vigderman, E. R. Zubarev and C. Jiang, *Langmuir*, 2012, **28**, 923–930.

10 C. G. Khoury and T. Vo-Dinh, *J. Phys. Chem. C*, 2008, **112**, 18849–18859.

11 R. Jin, Y. Charles Cao, E. Hao, G. S. Métraux, G. C. Schatz and C. A. Mirkin, *Nature*, 2003, **425**, 487–490.

12 Z. Fan, M. Bosman, X. Huang, D. Huang, Y. Yu, K. P. Ong, Y. A. Akimov, L. Wu, B. Li, J. Wu, Y. Huang, Q. Liu, C. Eng Png, C. Lip Gan, P. Yang and H. Zhang, *Nat. Commun.*, 2015, **6**, 7684.

13 C.-y. Zhang, Y. Lu, B. Zhao, Y.-w. Hao and Y.-q. Liu, *Appl. Surf. Sci.*, 2016, **377**, 167–173.

14 H. Parab, C. Jung, M.-A. Woo and H. G. Park, *J. Nanopart. Res.*, 2011, **13**, 2173–2180.

15 K. Jasuja and V. Berry, *ACS Nano*, 2009, **3**, 2358–2366.

16 Y. Ding, M. Chen and J. Erlebacher, *J. Am. Chem. Soc.*, 2004, **126**, 6876–6877.

17 R. M. Iost, M. V. A. Martins and F. N. Crespilho, *Ann. Acad. Bras. Cienc.*, 2019, **91**, DOI: 10.1590/0001-3765201920180817.

18 M. Pan, H. Sun, J. W. Lim, S. R. Bakaul, Y. Zeng, S. Xing, T. Wu, Q. Yan and H. Chen, *Chem. Commun.*, 2012, **48**, 1440–1442.

19 X. Bai and L. Zheng, *Cryst. Growth Des.*, 2010, **10**, 4701–4705.

20 Y. Shin, C. Lee, M.-S. Yang, S. Jeong, D. Kim and T. Kang, *Sci. Rep.*, 2014, **4**, 6119.

21 X. Wang, D. Yang, L. Chen, B. Liu, Z. Teng, N. He and Z. Wang, *Part. Part. Syst. Charact.*, 2018, **35**, 1800268.

22 H.-P. Ding, M. Wang, L.-J. Chen, W. Fan, Y.-I. Lee, D.-J. Qian, J. Hao and H.-G. Liu, *Colloids Surf., A*, 2011, **387**, 1–9.

23 T. Huang, F. Meng and L. Qi, *Langmuir*, 2010, **26**, 7582–7589.

24 W. Wang, Y. Han, M. Gao and Y. Wang, *CrystEngComm*, 2013, **15**, 2648–2656.

25 H.-L. Wu, C.-H. Chen and M. H. Huang, *Chem. Mater.*, 2009, **21**, 110–114.

26 J. Li, J. Wu, X. Zhang, Y. Liu, D. Zhou, H. Sun, H. Zhang and B. Yang, *J. Phys. Chem. C*, 2011, **115**, 3630–3637.

27 G. Frens, *Nat. Phys. Sci.*, 1973, **241**, 20–22.

28 X. Meng, A. Baride and C. Jiang, *Langmuir*, 2016, **32**, 6674–6681.

29 B. Ballarin, M. C. Cassani, D. Tonelli, E. Boanini, S. Albonetti, M. Blosi and M. Gazzano, *J. Phys. Chem. C*, 2010, **114**, 9693–9701.

30 W. Zhang, Q. Zhao and J. Yuan, *Angew. Chem., Int. Ed.*, 2018, **57**, 6754–6773.

31 B. Viswanath, P. Kundu, A. Halder and N. Ravishankar, *J. Phys. Chem. C*, 2009, **113**, 16866–16883.

32 H. Xia, S. Bai, J. Hartmann and D. Wang, *Langmuir*, 2010, **26**, 3585–3589.

33 J. R. Ansari, N. Singh, R. Ahmad, D. Chattopadhyay and A. Datta, *Opt. Mater.*, 2019, **94**, 138–147.

34 A.-L. Barabasi and R. Albert, *Science*, 1999, **286**, 509–512.

35 A.-L. Barabási and T. Vicsek, *Phys. Rev. A: At., Mol., Opt. Phys.*, 1990, **41**, 6881–6883.

36 A. Karperien, http://rsb.info.nih.gov/ij/plugins/fraclac/FLHelp/Introduction.htm, 1999–2013.

37 T. A. Witten and L. M. Sander, *Phys. Rev. B: Condens. Matter Mater. Phys.*, 1983, **27**, 5686–5697.

38 T. A. Witten and L. M. Sander, *Phys. Rev. Lett.*, 1981, **47**, 1400–1403.

39 Sirajuddin, A. Mechler, A. A. J. Torriero, A. Nafady, C.-Y. Lee, A. M. Bond, A. P. O'Mullane and S. K. Bhargava, *Colloids Surf., A*, 2010, **370**, 35–41.

40 E. Malel and D. Mandler, *J. Electrochem. Soc.*, 2008, **155**, D459–D467.

41 H. Tyagi, A. Kushwaha, A. Kumar and M. Aslam, *Nanoscale Res. Lett.*, 2016, **11**, 362.

42 N. Hau, P. Yang, C. Liu, J. Wang, P.-H. Lee and S.-P. Feng, *Sci. Rep.*, 2017, **7**, 39839.

43 T.-H. Lin, C.-W. Lin, H.-H. Liu, J.-T. Sheu and W.-H. Hung, *Chem. Commun.*, 2011, **47**, 2044–2046.

44 B. T. Draine and P. J. Flatau, *J. Opt. Soc. Am. A*, 1994, **11**, 1491–1499.

45 C. Sheng, X. Pengyu, L. Yue, X. Junfei, H. Song, O. Weihui, D. Yaping and N. Weihai, *Nano-Micro Lett.*, 2016, **8**, 328–335.

46 Y.-H. Lai, S.-C. Kuo, Y.-C. Hsieh, Y.-C. Tai, W.-H. Hung and U. S. Jeng, *RSC Adv.*, 2016, **6**, 13185–13192.

47 W. Han, E. Stepula, M. Philippi, S. Schlücker and M. Steinhart, *Nanoscale*, 2018, **10**, 20671–20680.

48 V. Sharma and V. Krishnan, *Sens. Actuators, B*, 2018, **262**, 710–719.

49 V. Sharma, R. Balaji, R. Walia and V. Krishnan, *Colloids Interface Sci. Ser.*, 2017, **18**, 9–12.

50 V. Sharma, S. Kumar, A. Jaiswal and V. Krishnan, *ChemistrySelect*, 2017, **2**, 165–174.

51 S. Nie and S. R. Emory, *Science*, 1997, **275**, 1102–1106.

52 C. Jiang, S. Markutsya and V. V. Tsukruk, *Langmuir*, 2004, **20**, 882–890.